

SASI ACTIVITY IN THREE-DIMENSIONAL NEUTRINO-HYDRODYNAMICS SIMULATIONS OF SUPERNOVA CORES

FLORIAN HANKE, BERNHARD MÜLLER, ANNOP WONGWATHANARAT, ANDREAS MAREK, HANS-THOMAS JANKA
Max-Planck-Institut für Astrophysik, Karl-Schwarzschild-Str. 1, 85748 Garching, Germany;
{fhanke,bjmuellr,annop,amarek,thj}@mpa-garching.mpg.de

Draft version March 26, 2013

ABSTRACT

The relevance of the standing accretion shock instability (SASI) compared to neutrino-driven convection in three-dimensional (3D) supernova-core environments is still highly controversial. Studying a $27 M_{\odot}$ progenitor, we demonstrate, for the first time, that violent SASI activity can develop in 3D simulations with detailed neutrino transport despite the presence of convection. This result was obtained with the PROMETHEUS-VERTEX code with the same sophisticated neutrino treatment so far used only in 1D and 2D models. While buoyant plumes initially determine the nonradial mass motions in the postshock layer, bipolar shock sloshing with growing amplitude sets in during a phase of shock retraction and turns into a violent spiral mode whose growth is only quenched when the infall of the Si/SiO interface leads to strong shock expansion in response to a dramatic decrease of the mass accretion rate. In the phase of large-amplitude SASI sloshing and spiral motions, the postshock layer exhibits nonradial deformation dominated by the lowest-order spherical harmonics ($\ell = 1, m = 0, \pm 1$) in distinct contrast to the higher multipole structures associated with neutrino-driven convection. We find that the SASI amplitudes, shock asymmetry, and nonradial kinetic energy in 3D can exceed those of the corresponding 2D case during extended periods of the evolution. We also perform parametrized 3D simulations of a $25 M_{\odot}$ progenitor, using a simplified, gray neutrino transport scheme, an axis-free Yin-Yang grid, and different amplitudes of random seed perturbations. They confirm the importance of the SASI for another progenitor, its independence of the choice of spherical grid, and its preferred growth for fast accretion flows connected to small shock radii and compact proto-neutron stars as previously found in 2D setups.

Subject headings: supernovae: general—hydrodynamics—instabilities—neutrinos

1. INTRODUCTION

Today there is a universal consensus in supernova theory that the neutrino-driven explosion mechanism hinges vitally on the supporting action of multidimensional hydrodynamic instabilities (with the notable exception of low-mass progenitors with O-Ne-Mg core; Kitaura et al. 2006). Two different hydrodynamical instabilities can potentially operate in the accretion flow between the stalled supernova shock and the forming neutron star: On the one hand, neutrino heating establishes a negative entropy gradient in the gain layer, which is unstable to buoyancy-driven convection, a fact that has long been recognized (Bethe 1990) and was confirmed already by the first generation of multi-dimensional simulations (Herant et al. 1992; Burrows & Fryxell 1992; Herant et al. 1994; Burrows et al. 1995; Janka & Müller 1996; Müller & Janka 1997). Later, purely hydrodynamical simulations of adiabatic accretion flows in the downstream region of a stalled shock (Blondin et al. 2003) revealed the existence of a distinctly different phenomenon, the “standing-accretion shock instability” (SASI), which involves large-scale $\ell = 1$ and $\ell = 2$ sloshing motions of the shock front and in three dimensions can also develop $\ell = 1, m = \pm 1$ spiral modes (Blondin & Mezzacappa 2007; Iwakami et al. 2009; Fernández 2010). The characteristic oscillatory growth of this instability is thought to be mediated by an amplifying advective-acoustic cycle (Foglizzo 2002; Foglizzo et al. 2006, 2007; Guilet & Foglizzo 2012; see, however, Blondin & Mezzacappa 2006 and Laming 2007

for the interpretation as a purely acoustic cycle). The hypothesis of an advective-acoustic process receives strong support by a detailed analysis of the mode frequencies (Scheck et al. 2008; Guilet & Foglizzo 2012) and by a shallow water analogue, the SWASI experiment, in which the water flow between a circular reservoir and a central tube as sink mimics the accretion flow that feeds the nascent neutron star (Foglizzo et al. 2012). With the role of the shock and of acoustic waves being played by a hydraulic jump and surface water waves, respectively, similar sloshing and spiral motions are observed as in the hydrodynamical simulations of collapsing stellar cores.

Violent hydrodynamic mass motions in the postshock layer do not only have the potential to improve the heating conditions in the supernova core by pushing the shock farther out and by prolonging the dwell time of the accreted matter in the heating region, which has supportive consequences for the supernova explosion (Herant et al. 1994; Burrows et al. 1995; Janka & Müller 1996; Fryer & Heger 2000; Marek & Janka 2009; Murphy & Burrows 2008; Nordhaus et al. 2010b; Hanke et al. 2012; Suwa et al. 2010). Convection and the SASI also create seed asymmetries that determine the ejecta morphology during the explosion phase (Kifonidis et al. 2003, 2006). Moreover, large-scale anisotropies in the ejecta may yield a natural explanation for the observed high kick velocities of young pulsars (Janka & Müller 1994; Herant 1995; Burrows & Hayes 1996; Scheck et al. 2004, 2006; Wongwathanarat et al. 2010b; Nordhaus et al. 2010a,

2012; Wongwathanarat et al. 2012). The $\ell = 1, |m| = 1$ spiral mode of the SASI could also provide an effective means for spinning up the proto-neutron star (PNS) (Blondin & Mezzacappa 2007). Moreover, large-amplitude SASI motions were found to stir strong g-mode activity in the neutron star surface, which leads to gravitational-wave emission (Marek et al. 2009; Murphy et al. 2009). Quasi-periodic variations of the accretion flow onto the neutron star due to SASI shock oscillations may also cause fluctuations of the radiated neutrino luminosities and mean energies (Marek et al. 2009; Ott et al. 2008; Brandt et al. 2011). The corresponding neutrino-signal fluctuations on millisecond timescales could be measured for a galactic supernova with good time resolution as, e.g., provided by the Ice-Cube detector (Lund et al. 2010, 2012) and could serve as valuable probe of neutrino properties (Ellis et al. 2012a,b) as well as of the dynamics in the supernova core.

Up to now most investigations of convection and the SASI in core-collapse supernovae have relied on axisymmetric (2D) simulations. Three-dimensional (3D) models based on various approximations for treating neutrino heating and cooling in the supernova core have only recently become available, but have already sparked a controversy about the development and mutual interaction of the two instabilities in 3D. Burrows et al. (2012) and Dolence et al. (2013), who conducted simulations using a simple light-bulb neutrino scheme, were rather outspoken in classifying the SASI as a subdominant phenomenon in the presence of neutrino heating. They argued that the violent sloshing motions seen in 2D neutrino-hydrodynamics simulations may be an artifact of the artificial symmetry assumption and are actually nothing but 2D convection in disguise. Murphy et al. (2012) also noted that nonlinear convection theory appears to explain the 3D flow properties of their models without the need of invoking the SASI as an additional instability. At first glance, these findings seem to be in line with other 3D studies relying on a similar light-bulb methodology (Iwakami et al. 2008; Nordhaus et al. 2010b; Hanke et al. 2012; Couch 2012) or on a gray neutrino transport approximation with chosen neutrino luminosities imposed at an inner grid boundary (Wongwathanarat et al. 2010b, 2012; Müller et al. 2012c). In contrast, Müller et al. (2012a) demonstrated by self-consistent, 2D, general relativistic (GR) simulations with sophisticated transport that genuine SASI activity remains possible for sufficiently small shock stagnation radius (caused by high mass accretion rates in the particular case of a $27M_{\odot}$ progenitor of Woosley et al. 2002). This suggests that details of the conditions may decide about the growth of the SASI, and that these conditions may not only depend on the properties of the progenitor star but also on the exact behavior of the stalled shock, which again depends on a reliable treatment of the neutrino physics. The mentioned 3D models might simply have missed the sweet spot for SASI growth in parameter space.

Recent Newtonian simulations by Takiwaki et al. (2012) and GR simulations by Kuroda et al. (2012) and Ott et al. (2012) are first, tentative steps to higher sophistication in 3D models, but these works were still focused on a few progenitors only and employed crude

neutrino transport methods with various simplifications concerning the description of neutrino propagation, of neutrino interactions, and of the energy dependence of the transport. Ott et al. (2012), using a neutrino leakage scheme and studying the same $27M_{\odot}$ progenitor as Müller et al. (2012a), observed low-level SASI activity at early times, which was eventually suppressed in models which exploded because of artificially enhanced neutrino heating. Their neutrino treatment, however, is not on par with the multi-group ray-by-ray-plus transport of Müller et al. (2012a) and therefore comparisons with the more sophisticated 2D models of Müller et al. (2012a) should be made only with great caution and reservation.

In view of the poor exploration of conditions in collapsing stellar cores in 3D so far and considering the substantial approximations that have been made in 3D supernova simulations until now, the strong opinions uttered about the dominance of neutrino-driven convection (Burrows et al. 2012; Murphy et al. 2012; Dolence et al. 2013) and the categorical rejection of an important role of the SASI in “realistic” 3D supernova models (Burrows 2013) are disturbing. Actually, it is not overly astonishing that the highly simplified setup investigated by these authors did not show signs of any pronounced SASI activity. The growth of SASI modes was clearly disfavored in their models by several aspects. Neglecting neutrino losses from the neutron star interior (above an optical depth of about unity) and using a relatively stiff nuclear equation of state the authors prevented the neutron star from shrinking below ~ 60 km. Correspondingly, the shock radius remained rather large, in which case the postshock velocities were relatively small and the advection timescale of the accretion flow through the gain layer was relatively long. This damped the development of the SASI, whose growth rate is roughly proportional to the inverse of the advection timescale (cf. Scheck et al. 2008). At the same time such conditions supported neutrino-driven convection, which preferably develops in the accretion flow for ratios χ of the advection time to the local buoyancy timescale above a critical value of $\chi \approx 3$ (Foglizzo et al. 2006).

Although the theoretical understanding of the growth conditions of the SASI and neutrino-driven convection is mostly based on linear theory (e.g., Foglizzo et al. 2007; Laming 2007; Yamasaki & Yamada 2007; Yamasaki & Foglizzo 2008; Guilet & Foglizzo 2012), the predictions were found to be consistent with the behavior seen in 2D hydrodynamical simulations of accretion shocks in collapsing stellar cores (Scheck et al. 2008) and in full-scale 2D supernova models (Müller et al. 2012a). Similarly, although it is *a priori* not clear whether the SASI sloshing motions (Blondin et al. 2003) and spiral modes (Blondin & Mezzacappa 2007; Fernández 2010) observed in adiabatic accretion flows in 2D and 3D, respectively, or in shallow-water experiments (Foglizzo et al. 2012), are conclusive for phenomena of relevance in the convectively unstable environment of the neutrino-heated layer, violent bipolar shock oscillations with SASI-typical characteristics were also identified to determine the evolution of the stalled supernova shock in some progenitors and preexplosion phases (e.g., Scheck et al. 2008; Müller et al. 2012a). While the phenomenon of the SASI as an advective-acoustic instability is not generically

linked to 2D, strong SASI activity has so far not been detected in full-scale 3D supernova simulations and it was speculated that its amplitude could be reduced by the kinetic energy being shared between three instead of two dimensions (Iwakami et al. 2008), that the absence of a flow-constraining symmetry axis might disfavor coherent mass motions of low spherical harmonics modes (Burrows 2013), or that neutrino-driven buoyancy is generally the fastest growing nonspherical instability in supernova cores (Burrows et al. 2012).

In this paper, we report about unambiguously identified SASI activity in the first 3D simulation with detailed neutrino transport of the $27 M_{\odot}$ progenitor model that was investigated by Müller et al. (2012a). For this 3D simulation we employed the PROMETHEUS-VERTEX neutrino-hydrodynamics code with detailed ray-by-ray-plus neutrino transport and the sophisticated treatment of energy-dependent neutrino interactions also applied in previous 2D simulations with this code (e.g., Buras et al. 2006b; Marek & Janka 2009) and in the 2D GR models of Müller et al. (2012b,a, 2013). Contrary to the claims discussed above, our model shows that despite the presence of neutrino-driven convection, the SASI can grow no less vigorously in 3D (without any coordinate grid-imposed symmetry) than in 2D as long as small shock radii are maintained (in the $27 M_{\odot}$ star because of high mass accretion rates) and guarantee favorable growth conditions. We also observe the development of a clear spiral mode. SASI shock motions appear to be diminished only when the accretion rate drops after the Si/SiO shell interface reaches the shock and the shock is able to expand to considerably larger radii. The variation of the relative strengths of neutrino-driven convection and SASI sloshing is consistent with experience and understanding based on previous 2D simulations. In order to demonstrate this more directly we also performed parametric 2D and 3D core-collapse and explosion simulations by using simplified, gray neutrino transport as in Müller et al. (2012c) and Wongwathanarat et al. (2010b, 2012) to enhance the computational efficiency. Excising the high-density core and replacing it by a contracting inner boundary condition, at which neutrino luminosities with chosen values could be imposed, allowed us to control the supernova core conditions. In these simulations we studied a $25 M_{\odot}$ progenitor and made use of an axis-free Yin-Yang grid (Wongwathanarat et al. 2010a) instead of a polar grid. These simulations did not only show that the discussed SASI phenomenon can play a role in different progenitor stars and is not dependent on the choice of a particular computational grid, they also confirmed that SASI mass motions in 3D can be triggered by the same conditions that are known to be favorable in 2D.

Our paper is structured as follows. In Sect. 2 we discuss the results of our fully self-consistent neutrino-hydrodynamics simulation of the $27 M_{\odot}$ progenitor, describe briefly the numerical methods and modeling setup, analyze differences of the convective and SASI activity between 2D and 3D simulations, and present evidence for the temporary development of a spiral mode. In Sect. 3 we compare 2D and 3D results for three simulations of the $25 M_{\odot}$ model with our simplified modeling setup, whose main features we also summarize before we investigate the dependence of the development of SASI

activity on the parametrically regulated conditions in the postshock and neutrino-heating layer. A discussion and conclusions will follow in Sect. 4.

2. FULLY SELF-CONSISTENT 3D CORE-COLLAPSE SIMULATION OF A $27 M_{\odot}$ STAR

2.1. Numerical methods and modeling setup

The calculations for the $27 M_{\odot}$ model in 2D and 3D were performed with the elaborate neutrino-hydrodynamics code PROMETHEUS-VERTEX. This supernova simulation tool combines the hydrodynamics solver PROMETHEUS (Fryxell et al. 1989), which is a dimensionally-split implementation of the piecewise parabolic method (PPM) of Colella & Woodward (1984), with the neutrino transport module VERTEX (Rampp & Janka 2002). VERTEX solves the energy-dependent moment equations for the neutrino energy and momentum density (with full velocity dependence) for spherically symmetric transport problems defined to be associated with every angular bin of the polar grid (“radial rays”) used for the multi-dimensional simulations. The moment equations are closed by a variable Eddington factor relation that is provided by the formal solution of a model Boltzmann equation. An up-to-date set of neutrino interaction rates is included in VERTEX (see, e.g., Müller et al. 2012b). In the multi-dimensional case, our ray-by-ray-plus approach (Buras et al. 2006b) includes non-radial neutrino advection and pressure terms in addition to the radial transport solves. In the simulations presented here, we assume monopolar gravity, but include general relativistic corrections by means of an effective gravitational potential (Marek et al. 2006).

We simulate the evolution of the $27 M_{\odot}$ progenitor of Woosley et al. (2002), which was previously investigated by Müller et al. (2012a) and Ott et al. (2012), both in 2D and in 3D, using the high-density equation of state (EoS) of Lattimer & Swesty (1991) with a nuclear incompressibility of $K = 220$ MeV. The models are computed on a spherical polar coordinate grid with an initial resolution of $n_r \times n_{\theta} \times n_{\varphi} = 400 \times 88 \times 176$ (3D) and $n_r \times n_{\theta} = 400 \times 88$ (2D) zones. Later, refinements of the radial grid ensure adequate resolution in the PNS surface region. The innermost 10 km are computed in spherical symmetry in both cases to avoid excessive time-step limitations. Seed perturbations for aspherical instabilities are imposed by hand 10 ms after bounce by introducing random perturbations of 0.1% in density on the whole computational grid.

2.2. SASI activity: 2D versus 3D

While both the SASI and convection can lead to large-scale shock deformations, the SASI is distinguished by a characteristic oscillatory growth and in its nonlinear stage by the quasi-periodic, oscillatory nature of the shock motions. In 2D, the artificial symmetry constraint and the excitation of large-scale modes by the inverse turbulent cascade could still produce a quasi-periodic sloshing motion even in convectively-dominated models (Burrows et al. 2012), and a more refined analysis is necessary to identify the SASI (Müller et al. 2012a). However, in 3D the distinction is much clearer, since large-scale shock deformations caused by buoyancy-driven convection initially evolve randomly without any identifiable periodicity and then grow *monotonically* once they reach

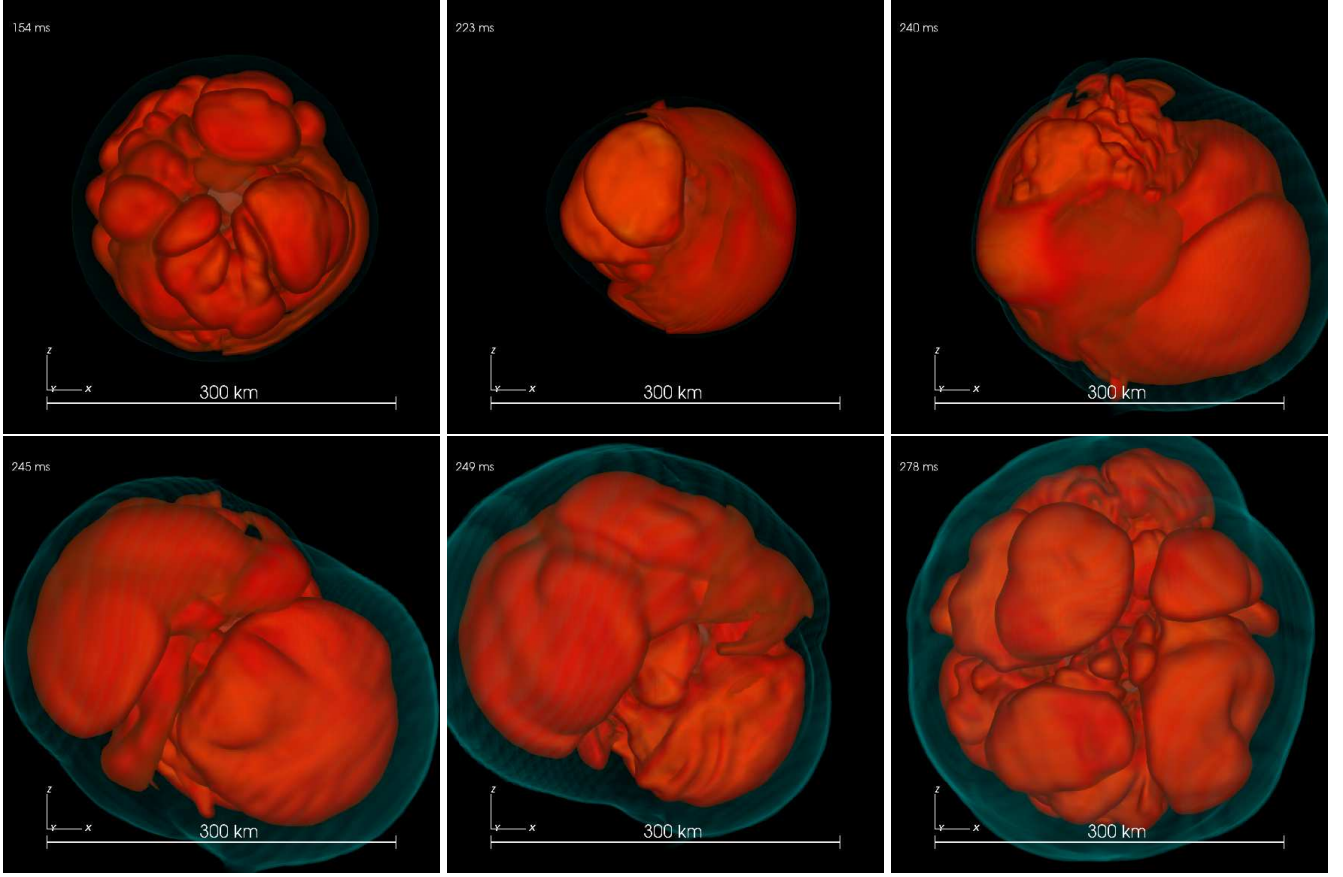


Figure 1. Snapshots of phases with convective and SASI activity in the evolution of the $27 M_{\odot}$ model at 154 ms, 223 ms, 240 ms (upper panels, from left to right), 245 ms, 249 ms, and 278 ms (lower panels, from left to right). The volume rendering visualizes surfaces of constant entropy: The outer, bluish, semi-transparent surface is the supernova shock, the red surfaces are entropy structures in the postshock region. The upper left panel displays mushroom-like plumes of expanding, high-entropy matter that are typical of neutrino-driven buoyancy. The upper middle and right plots and the lower left and middle panels show distinctly different entropy structures of dipolar (and quadrupolar) asymmetry, which engulf the still visible buoyant plumes with their higher-order spherical harmonics mode pattern. The entropy asymmetries of $\ell = 1, 2$ character are caused by global shock sloshing motions, which create hemispheric high-entropy shells in phases of shock expansion. At 223 ms and 240 ms the shock has pushed towards the lower right corner of the panels whereas at 245 ms and 249 ms it is in a phase of violent expansion motion towards the upper left corner of the plots. All stages exhibit a strong deformation of the shock. At 278 ms the vivid SASI phase is over, the shock is more spherical again, and the postshock entropy structures correspond to neutrino-driven plumes.

a certain threshold amplitude (Burrows et al. 2012). Periodic SASI oscillations and large-scale shock deformations caused by convection can therefore hardly be mistaken for each other in 3D.

Images of the entropy distribution in the postshock layer (Figure 1) and in particular the corresponding movie of our 3D simulation of the $27 M_{\odot}$ progenitor indeed provide a clear hint that both distinctly different instabilities are at work in the shocked accretion flow around the nascent neutron star. The instabilities develop nearly at the same time and are present simultaneously for an extended period of the simulated postbounce evolution. The first small mushroom-like Rayleigh-Taylor fingers of neutrino-driven convection become visible around 80–100 ms after bounce to subsequently grow stronger and larger in angular size over a timescale of some ten milliseconds. At about 125 ms p.b. the rising plumes begin to cause shock deformation and a modest amount of global asphericity of the accretion layer. Until ~ 155 ms the activity in the postshock layer is clearly dominated by neutrino-driven buoyancy (Figure 1, upper left panel), but at $t \gtrsim 155$ ms, during a phase

of accelerated shock recession, coherent entropy structures show up first. The corresponding low-mode spherical harmonics pattern clearly differs from the buoyant mushrooms on smaller angular scales. This phenomenon is associated with shock oscillations, which quickly amplify to bipolar shock sloshing motions and create characteristic, hemispheric high-entropy shells during phases of fast shock expansion. These half-shells of shock-heated matter engulf the buoyant bubbles of neutrino-driven convection in deeper regions (Figure 1, upper middle and right and lower left and middle panels). While the sloshing axis initially wanders, it becomes more stable as the SASI sloshing of the shock further grows in amplitude and violence between ~ 195 ms and ~ 240 ms. As a consequence, an expansion of the average shock radius is driven even before the Si/SiO composition-shell interface arrives at the shock and the mass accretion rate starts to drop steeply at $t \sim 220$ ms (Figure 2, upper left panel). The decrease of the accretion rate supports the shock expansion, in course of which the bipolar, quasi-periodic shock pulsations gain even more power. At $t \sim 225$ ms a spiral mode seems to set in for several revolutions be-

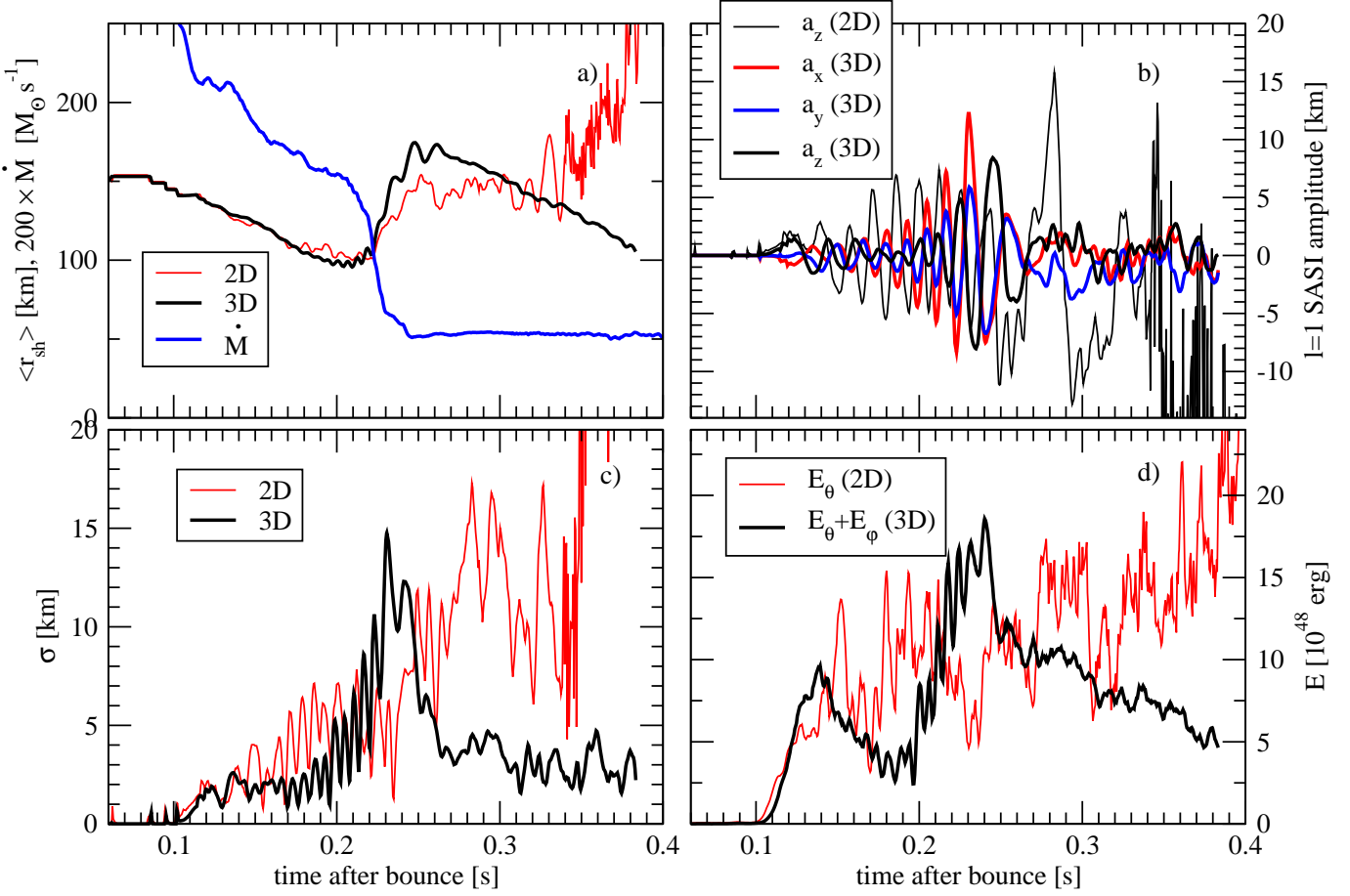


Figure 2. Comparison of SASI activity and shock evolution in the 2D and 3D simulations of the \$27 M_\odot\$ model. *Panel a:* average shock radius ($\langle r_{\text{sh}} \rangle = a_0$) and mass accretion rate of the collapsing stellar core at 400 km; *panel b:* components of the SASI $\ell = 1$ amplitude vector; *panel c:* rms shock deformation σ ; *panel d:* kinetic energy of non-radial mass motions in the gain layer.

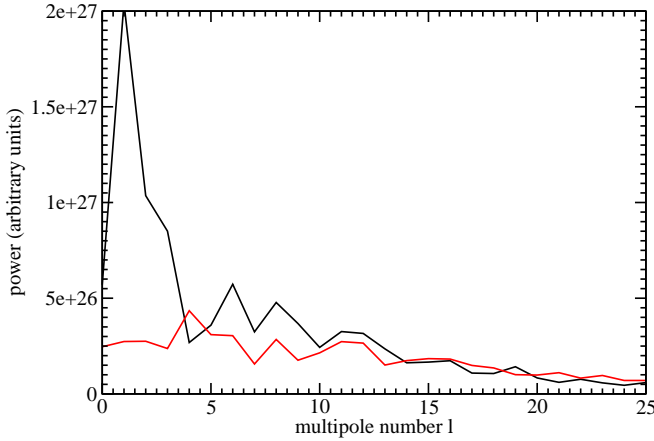


Figure 3. Power spectra of v_ϕ of the \$27 M_\odot\$ 3D model sampled between $r = 63$ km and 80 km at post-bounce times of 222 ms (black) and 259 ms (red). At 222 ms, the strong SASI produces a distinctive peak at $l = 1$, which is absent during the later, convection-dominated phase.

fore the average shock radius reaches its maximum extension at \$\sim 250\$ ms and the SASI sloshing dies off at \$t \gtrsim 260\$ ms. The presence of large-amplitude spiral motions is reflected by considerable variations of the mean shock radius between 230 ms and 260 ms. These disappear when the SASI activity ceases at \$t \sim 260\$ ms (Fig-

ure 2, upper left panel). Later on, until the end of our 3D simulation, aspherical mass motions in the postshock layer are dominated again by the buoyant plumes typical of neutrino-driven convection (Figure 1, lower right panel).

This verbal description of the dynamical evolution of the postshock accretion layer is supported by a detailed analysis based on several time-dependent parameters that quantify the characteristic features of SASI activity. To this end we perform a time-dependent decomposition of the angle-dependent shock position $r_{\text{sh}}(\theta, \varphi)$ into spherical harmonics Y_ℓ^m :

$$a_\ell^m = \frac{(-1)^{|m|}}{\sqrt{4\pi(2\ell+1)}} \int_\Omega r_{\text{sh}}(\theta, \varphi) Y_\ell^m(\theta, \varphi) d\Omega. \quad (1)$$

Here the Y_ℓ^m are real spherical harmonics with the same normalization as used by Burrows et al. (2012) and Ott et al. (2012). With this choice of basis functions, the coefficients with $\ell = 1$ give the angle-averaged Cartesian coordinates of the shock surface,

$$a_1^{-1} = \langle y_{\text{sh}} \rangle =: a_y, \quad a_1^0 = \langle z_{\text{sh}} \rangle =: a_z, \quad a_1^1 = \langle x_{\text{sh}} \rangle =: a_x, \quad (2)$$

and a_0^0 is just the average shock-radius $\langle r_{\text{sh}} \rangle$.

The time evolution of the coefficients a_x , a_y (3D), and a_z (3D and 2D) is shown in panel b of Figure 2. Both in 2D and in 3D, the shock surface clearly oscillates in

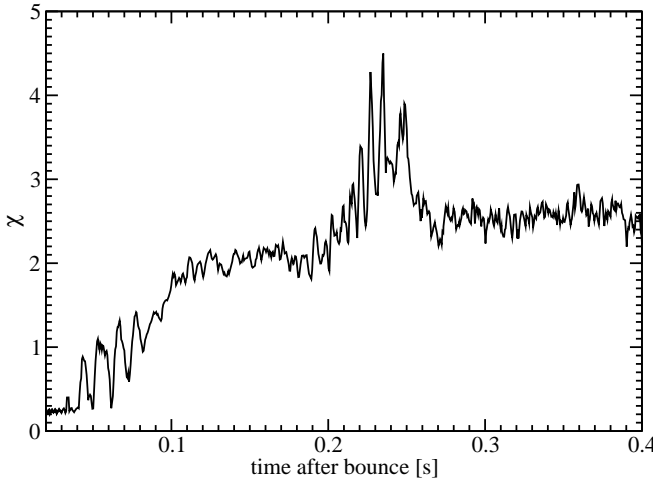


Figure 4. Evolution of the stability parameter χ for the gain layer of the 3D simulation of the $27 M_{\odot}$ progenitor. During most of the time $\chi < 3$. This suggests conditions in the postshock accretion flow which disfavor the growth of neutrino-driven convection relative to the development of the SASI in analogy to the 2D model discussed by Müller et al. (2012a).

a quasi-periodic manner until ~ 260 ms after bounce, i.e. until shortly after the Si/SiO shell interface has reached the shock and the accretion rate has dropped considerably between ~ 220 ms and 240 ms p.b. The lower accretion rate results in a pronounced expansion of the average shock radius (panel a of Figure 2), which initially is stronger in 3D. However, the 2D model maintains large (albeit less regular) shock oscillations, with the average shock radius eventually overtaking the 3D model at ~ 300 ms when an explosion develops (i.e. somewhat later than in the GR simulation of Müller et al. 2012a)¹. By contrast, the shock continues to recede in the 3D run. The more optimistic evolution of the 2D model compared to the failing 3D model at late stages is consistent with the findings of Hanke et al. (2012), and could be due to the action of the inverse turbulent energy cascade, which continues to feed energy into large-scale modes in 2D.

However, the evolution of the two simulations prior to the infall of the Si/SiO interface is remarkable: While the amplitude of the $\ell = 1$ mode is initially larger in 2D, the individual components a_x , a_y , and a_z of the $\ell = 1$ amplitude vector in 3D become comparable to a_z in 2D around 200 ms, and a_x even reaches considerably bigger values. During this phase, the SASI is undoubtedly *stronger* in 3D than in 2D. Further confirmation of this assessment is provided by the root-mean-square deviation $\sigma(r_{\text{sh}})$ of the shock radius from its average value (panel c of Figure 2):

$$\sigma = \sqrt{(4\pi)^{-1} \int (r_{\text{sh}}(\theta, \varphi) - \langle r_{\text{sh}} \rangle)^2 d\Omega} \quad (3)$$

For reasonably small amplitudes, σ is also a measure for

¹ It is not clear whether this difference or how much of this difference is caused by GR effects, because the models in the present paper were simulated with a slightly different treatment of the low-density equation of state, which led to a significant delay (~ 35 ms) of the infall of the silicon layer and a correspondingly later arrival of the Si/SiO shell interface at the shock.

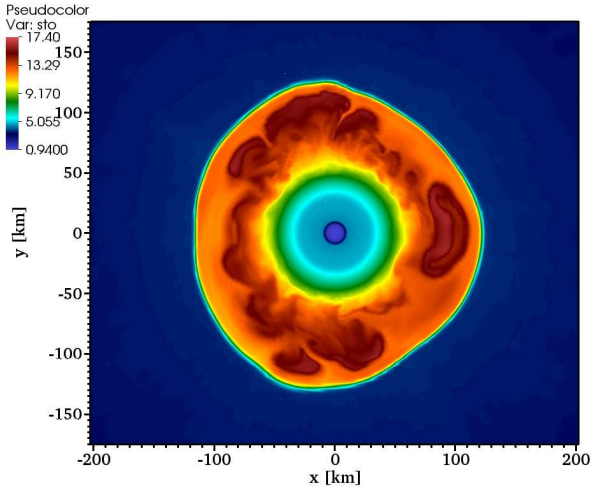


Figure 5. Snapshot of the entropy (color coded according to color bar at the upper left corner, in units of Boltzmann's constant k_B per nucleon) in the plane through the origin normal to the vector $\mathbf{n} = (-0.35, 0.93, 0.12)$ at a post-bounce time of 152 ms in the $27 M_{\odot}$ 3D model. The high-entropy plumes with high-order spherical harmonics pattern suggest buoyancy-driven convective overturn of neutrino-heated matter.

the total power of SASI amplitudes with different ℓ :

$$\sigma \approx \sqrt{\sum_{\ell=1}^{\infty} \sum_{m=-\ell}^{\ell} |a_{\ell}^m|^2}. \quad (4)$$

The same picture emerges when we consider the kinetic energies E_{θ} and E_{φ} associated with motions in the θ - and φ -directions in the gain region,

$$E_{\theta} = \frac{1}{2} \int_{V_{\text{gain}}} \rho v_{\theta}^2 dV, \quad E_{\varphi} = \frac{1}{2} \int_{V_{\text{gain}}} \rho v_{\varphi}^2 dV. \quad (5)$$

As shown in panel d of Figure 2, the total energy contained in non-radial motions is also larger in 3D during the relevant phase around ~ 230 ms. In the period of continuous increase of the SASI amplitude in the 3D model between $t \sim 155$ ms and ~ 240 ms, the kinetic energy grows and σ exhibits quasi-periodic modulations signaling the shock sloshing motions. Interestingly, during the phase of strongest SASI activity we find rough equipartition between the kinetic energies of non-radial motions $E_{\theta} + E_{\varphi}$, and the energy E_r contained in fluctuating radial velocities,

$$E_r = \frac{1}{2} \int_{V_{\text{gain}}} \rho (v_r - \langle v_r \rangle)^2 dV, \quad (6)$$

where $\langle v_r \rangle$ is the angle-averaged radial velocity. This equipartition is apparently not a unique feature of buoyancy-driven turbulence (cf. Murphy et al. 2012), at least not as far as these volume-integrated quantities are concerned.

A clear difference between SASI dominated and convection dominated phases of the $27 M_{\odot}$ 3D model can be observed in the power spectrum of the azimuthal velocity v_{φ} as a function of multipole order ℓ . Figure 3 shows the spectra during a SASI active phase (222 ms p.b.) compared to the later time (259 ms) when the SASI

motions cease and convective plumes with their higher-order multipole pattern determine the asphericities in the postshock region again. The power spectra are evaluated with equation (8) of Hanke et al. (2012) for v_φ (weighted with the square root of the density) integrated over a radial region between 63 km and 80 km. The presence of the SASI low-mode deformation at 222 ms leads to a prominent peak of the power spectrum at low multipole orders, which is absent in the later spectrum.

The shock deformation and SASI amplitude moderately increase as the shock retreats between ~ 100 ms and 200 ms p.b. (The same is true for the specific nonradial kinetic energy in the gain layer, although the kinetic energy decreases temporarily because of the decreasing mass in the gain region.) It is noteworthy that the few tens of milliseconds of stronger SASI activity in 3D coincide with a phase of more rapid shock expansion than in 2D. Conceivably, the more energetic SASI motions provide a stronger push against the pre-shock ram pressure. A close examination of the $\langle r_{\text{sh}} \rangle$ in Figure 2 shows that some (oscillatorily modulated) SASI-aided shock expansion seems to set in around 190 ms, i.e. already before the rapid drop of the preshock mass-accretion rate that begins at ~ 220 ms. Therefore one might speculate that with slightly more time available for the growth of the SASI, the extra support by nonradial SASI motions might have driven the 3D model over the threshold for a neutrino-powered runaway expansion of the shock after the infall of the Si/SiO interface.

Quite remarkably, the SASI is not only able to reach larger amplitudes in 3D than in 2D as long as its growth conditions remain favorable, but it is even found to develop *despite* some earlier convective activity. Figure 4 displays the critical parameter χ for the growth of convection as evaluated from spherically averaged stellar quantities in the gain layer of our 3D simulation of the $27 M_\odot$ progenitor according to equation (3) in Müller et al. (2012a),

$$\chi = \int_{\langle r_g \rangle}^{\langle r_{\text{sh}} \rangle} \frac{\text{Im } \omega_{\text{BV}}}{|\langle v_r \rangle|} dr, \quad (7)$$

where ω_{BV} is the Brunt-Väisälä frequency. The integration is performed between the average gain radius $\langle r_g \rangle$ and the average shock radius $\langle r_{\text{sh}} \rangle$. Note that only regions contribute to the integral where $\omega_{\text{BV}}^2 < 0$ indicates local instability. The parameter χ roughly measures the ratio between the advection timescale of the flow through the gain layer and the growth timescale of convection. Since perturbations are advected out of the gain layer with the accretion flow in a finite time, convection can develop only when perturbations are amplified sufficiently strongly within this time. For the linear regime (i.e., for small initial perturbations) Foglizzo et al. (2006) found the threshold condition of $\chi \gtrsim 3$ for convective activity to develop in the accretion flow of the gain layer. This result of mathematical analysis is supported by numerical studies in 2D by Buras et al. (2006a); Scheck et al. (2008); Fernández & Thompson (2009b,a).

Despite $\chi < 3$ (Figure 4), however, convection develops around 80 ms after bounce in our 3D simulation of the $27 M_\odot$ model. This happens because convective activity is not only seeded by the artificially imposed, random density perturbations of 0.1% amplitude (cf. Sect. 2.1)

but also by numerical perturbations along the axis of the computational polar grid in one hemisphere, which we are not able to damp perfectly. Although still small, these numerical effects are sufficiently large to trigger the rise of a buoyant plume against the advection flow, which instigates further perturbations that exceed the linear regime. In this case convection can be initiated although $\chi < 3$ signals stability according to linear analysis (Foglizzo et al. 2006). We note in passing that the level of seed perturbations was smaller and well compatible with linear theory in the 2D models of Müller et al. (2012a), and we also emphasize that the axial perturbations have a noticeable effect only in the early growth phase of convection whereas no significant axial artifacts or alarming flow perturbations near the polar axis can be observed during the later phases of fully developed nonradial flow activity in the postshock flow (see Figure 1). Once strong SASI and convective mass motions have developed in the flow, the supernova core contains a noise level so high that a subsequent decline of χ below the critical threshold of ~ 3 does not imply that convective activity is unable to continue (Müller et al. 2012a).

Figure 5 shows a snapshot of the entropy in a 2D slice at 152 ms. Here, the post-shock flow is still dominated by multiple, intermediate-scale plumes as familiar from buoyancy-driven convection. SASI shock sloshing becomes strong and temporarily dominant only afterward. The argument that any convective activity arising from sufficiently large seed perturbations will quench the SASI thus seems to be invalid. The competition between convection and the SASI is obviously more subtle than a superficial reading of recent papers (Burrows et al. 2012; Murphy et al. 2012; Müller et al. 2012a; Ott et al. 2012) might suggest. Some relevant aspects of the competing growth conditions and interaction of the two instabilities were discussed on the basis of 2D supernova simulations by Scheck et al. (2008). A very similar behavior can be diagnosed in the 3D case and will be addressed on the basis of parametric 3D studies in Sect. 3, where we will make use of an axis-free Yin-Yang grid in order to avoid the perturbative influence of the polar coordinate axis during the linear growth phase of the seed perturbations.

2.3. Detecting the spiral mode of the SASI

While the SASI is limited to a sloshing motion along the symmetry axis in 2D, there is the possibility of a spiral mode in 3D (Blondin & Mezzacappa 2007; Iwakami et al. 2009; Fernández 2010), which could provide a means for angular momentum separation between the PNS and the ejecta, and might also have different saturation properties in the non-linear phase.

Detecting the spiral mode is not straightforward, as the time evolution of the coefficients a_ℓ^m needs to be taken into account. Merely computing the coefficients with $m \neq 0$ is *not* sufficient. In principle, spiral and sloshing modes can be disentangled by a Fourier analysis of $a_\ell^m(t)$ (Iwakami et al. 2008) if they remain stable over several oscillation periods. We use a somewhat different approach to visualize the character of the $\ell = 1$ mode in our 3D model here. The coefficients a_1^m can be combined into a vector,

$$\mathbf{a}_1 = (a_1^1, a_1^{-1}, a_1^0) = (a_x, a_y, a_z), \quad (8)$$

which is a rough measure of the angle-averaged displace-

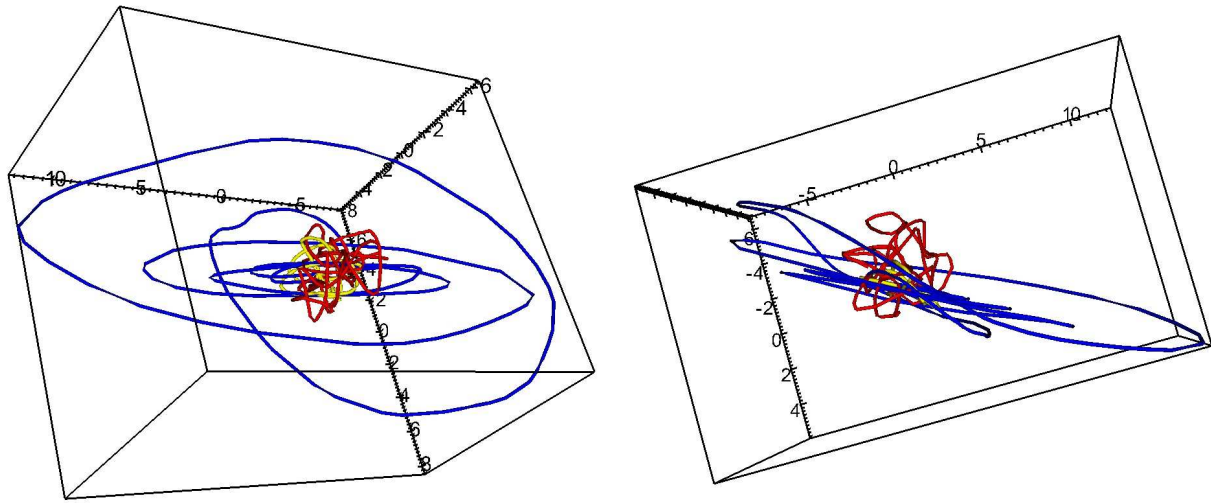


Figure 6. Evolution of the $\ell = 1$ amplitude vector \mathbf{a}_1 for the $27 M_\odot$ simulation from two different viewing angles. Different colors are used for the phase up to 177 ms (yellow), the phase of strong SASI activity (blue, up to 265 ms), and the late, SASI-quiet phase (red).

ment of the shock center from the origin and also indicates the direction and amplitude of the shock deformation (neglecting modes with higher ℓ). We visualize the time evolution of this amplitude vector in 3D space in Figure 6 with different colors of the trajectory indicating different phases of the simulation.

Once the SASI starts to grow vigorously (blue curve), \mathbf{a}_1 initially moves along a narrow elliptical path with growing semi-major axis, indicating a predominant sloshing mode. Towards the phase of strongest SASI activity, the trajectory becomes more circular, signaling the transition to a spiral mode. The plane of the spiral remains relatively stable until the maximum amplitude is reached and the SASI dies down again. It is roughly perpendicular to the vector $\mathbf{n} = (-0.35, 0.93, 0.12)$, i.e. there is no alignment with the axis of the spherical polar grid. Figure 6 also further illustrates the different behavior during the “SASI-dominated” phase compared to the earlier and later “convectively-dominated” phases, during which \mathbf{a}_1 evolves in a more random fashion.

Slicing the model along the plane in which \mathbf{a}_1 predominantly moves allows us to visualize the distinctive spiral mode pattern, as shown in Figure 7. The snapshots of the rotational velocity around the “axis” of the spiral mode (in the plane through the origin perpendicular to that axis) reveal two counter-rotating regions. While these regions are initially of comparable size, the flow in the counter-clockwise direction eventually dominates, and the rotation of the mode pattern with a continuously shifting triple point can clearly be seen.

During the short phase of strong SASI activity, angular momentum separation by the spiral mode proceeds very efficiently, transferring a total angular momentum of $\sim 5 \times 10^{46}$ erg s into the gain region (Figure 8). As expected, the direction of the angular momentum vector is extremely similar to the normal vector of the spiral plane. However, all the angular momentum is eventually advected out of the gain region after the SASI has died down.

3. PARAMETRIC 2D AND 3D POST-BOUNCE SIMULATIONS OF A $25 M_\odot$ STAR

In order to probe the SASI growth conditions and the differences between 2D and 3D accretion flows in more detail, we performed a set of simulations for the $25 M_\odot$ solar-metallicity progenitor of Woosley et al. (2002). The choice of this stellar model is motivated by the fact that it turned out to be particularly hard to explode in self-consistent 2D simulations with sophisticated neutrino treatment, where it exhibits violent shock sloshing motions with amazingly stable periodicity over a long period of postbounce evolution (Müller et al. 2013; Janka et al. 2012). It thus offers promising perspectives to explore the relevance of the SASI in 3D for a second progenitor in addition to the $27 M_\odot$ case investigated in Sect. 2.

3.1. Numerical methods and modeling setup

In order to efficiently run several 3D simulations, a simplified setup is employed that was extensively applied before by Wongwathanarat et al. (2010b, 2012); Müller et al. (2012c); Scheck et al. (2006, 2008); Arcones et al. (2007); Arcones & Janka (2011). Instead of the elaborate neutrino transport solver used for the $27 M_\odot$ run in Sect. 2, now an approximate, gray (ray-by-ray) neutrino transport is used (for details, see Scheck et al. 2006). Moreover, the high-density interior of the proto-neutron star (at densities above neutrino optical depths between some 10 and several 100, depending on the phase of the evolution) is excised and replaced by an inner grid boundary (also in contrast to the $27 M_\odot$ run, where the whole neutron star was included in the simulation). A contraction of the boundary radius is prescribed to mimic the shrinking neutron-star core (Scheck et al. 2006; Arcones et al. 2007), and neutrino luminosities of chosen magnitude and time dependence are imposed there to parametrize the neutrino losses from the interior core volume. The transport approximation allows us to account for radial flux variations due to accretion luminosity and neutrino energy deposition in the

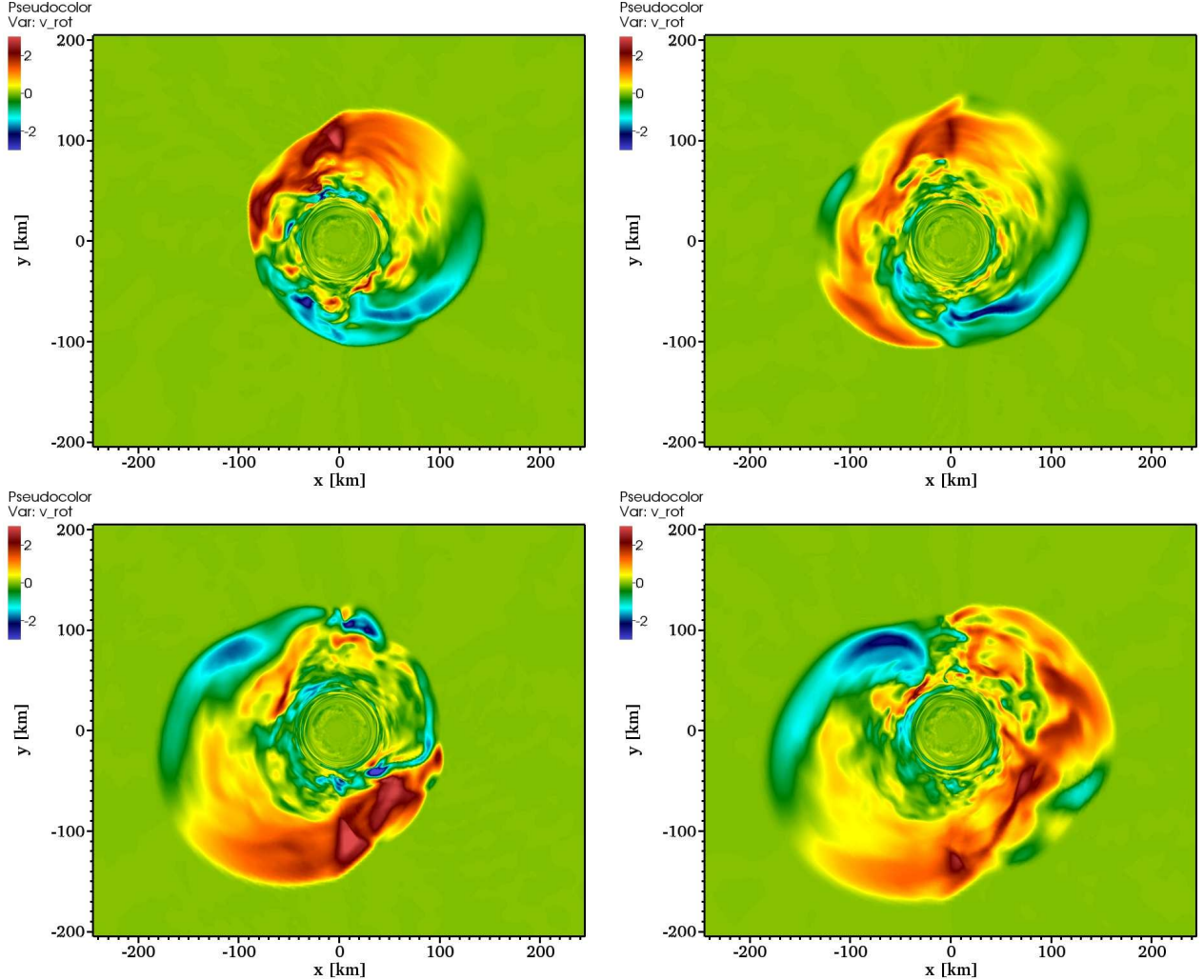


Figure 7. Snapshots of the rotational velocity around the origin in the plane perpendicular to $\mathbf{n} = (-0.35, 0.93, 0.12)$ at post-bounce times of 223 ms, 227 ms, 231 ms, and 235 ms during the 3D simulation of the $27 M_{\odot}$ progenitor. Red and yellow (positive velocity values) correspond to counterclockwise rotation.

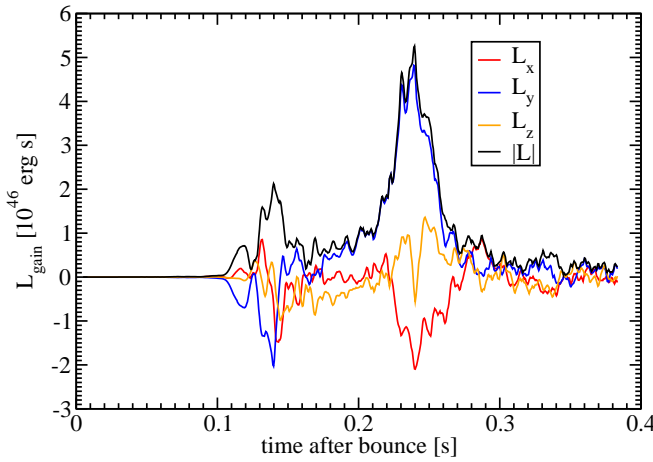


Figure 8. Time evolution of the angular momentum components L_x , L_y , and L_z , and of the absolute magnitude $|L|$ of the total angular momentum contained in the gain region of the $27 M_{\odot}$ simulation in 3D.

gain layer. Although this modeling approach is not elaborate enough to exactly reproduce the results obtained

with more sophisticated and fully consistent treatments, it nevertheless includes a reasonably good representation of all aspects that determine the flow dynamics in collapsing stellar cores. The parametrized approach has the big advantage that different components can be controlled to a large extent independently so that studies with varied conditions can be performed in a systematic manner.

The computational efficiency is further enhanced by the use of an axis-free Yin-Yang grid (Wongwathanarat et al. 2010a), which avoids the time-step constraints and numerical artifacts close to the axis of the polar grid. The 3D runs were conducted with a grid zoning of $600(r) \times 47(\theta) \times 137(\varphi) \times 2$, the corresponding 2D models with $600(r) \times 90(\theta)$ zones, which ensures an angular resolution of 2° in both 2D and 3D. The inner grid boundary is placed at an enclosed mass of approximately $1.1 M_{\odot}$. When the models are started from 1D conditions at 15 ms after bounce, the corresponding initial radius of the inner grid boundary, R_{ib} , is located at 53 km, while the radius of the outer grid boundary, R_{ob} , is chosen to be at 10000 km in the beginning. The radial grid resolution, Δr , is kept constant at 0.265 km up to the

radius of initially 100 km, beyond which the zone width is increased logarithmically.

The shrinking core of the nascent neutron star is described by the contraction of the inner grid boundary according to equation (1) of Scheck et al. (2006) with an exponential timescale of $t_{\text{ib}} = 1$ s and a final radius of R_{ib}^{f} . Along with the retraction of the inner grid boundary the whole radial grid is moved with the same velocity. During the computed model evolution the neutrino luminosities imposed at the inner grid boundary are kept constant. The mean neutrino energies of the neutrino fluxes entering the grid are prescribed as functions of the temperature in the first radial cell of the computational grid as described by Ugliano et al. (2012).

In order to trigger the growth of nonradial hydrodynamic instabilities, seed perturbations with randomly varied amplitude are imposed as zone-to-zone variations of the radial velocity in the whole computational domain at the start of the 2D or 3D simulations.

We present results of three types of models, which differ in the size of the seed perturbations, either of 0.1% or 3% amplitude (“small” and “large” initial perturbations, respectively), and in the contraction behavior adopted for the neutron-star core. The latter is controlled by the assumed asymptotic radius of the inner grid boundary at $t \rightarrow \infty$, namely $R_{\text{ib}}^{\text{f}} = 15$ km for “slow contraction” and $R_{\text{ib}}^{\text{f}} = 10$ km for “fast contraction”. In the case of slow contraction the imposed boundary luminosities of ν_e and $\bar{\nu}_e$ are 1.49×10^{51} erg s $^{-1}$ and 0.89×10^{51} erg s $^{-1}$, respectively; in the case of fast contraction we use $L_{\nu_e, \text{ib}} = 5.96 \times 10^{51}$ erg s $^{-1}$ and $L_{\bar{\nu}_e, \text{ib}} = 3.58 \times 10^{51}$ erg s $^{-1}$. (Muon and tau neutrinos and antineutrinos are included as well but do not play an important role for the hydrodynamics of the accretion flow in the supernova core.) The three computed models are characterized by the following parameter sets:

- S25-1:** slow boundary contraction, 3% perturbation amplitude;
- S25-2:** fast boundary contraction, 0.1% perturbation amplitude;
- S25-3:** fast boundary contraction, 3% perturbation amplitude.

Model S25-1 was evolved until 515 ms after bounce, while S25-2 and S25-3 were run until 365 ms after core bounce.

3.2. SASI activity in dependence of supernova-core conditions

Figure 9 provides an overview of the dynamical evolution of the three models S25-1, S25-2, and S25-3 in 2D compared to 3D by showing the north polar and south polar entropy profiles of the 2D simulations in the top panels, shock radii (average, maximum, minimum) in the second line from the top, the critical χ parameter (evaluated according to Equation 7) in the panels of the third line, and a spherical harmonics mode decomposition of the deformed shock surface in the fourth and fifth lines for 2D and 3D cases, respectively.

Here we follow the deformation mode analysis used by Wongwathanarat et al. (2012) and write the time-dependent decomposition of the 3D shock surface,

$r_{\text{sh}}(\theta, \varphi)$, in spherical harmonics as

$$r_{\text{sh}}(\theta, \varphi) = \sum_{\ell=0}^{\infty} \sum_{m=-\ell}^{\ell} b_{\ell}^m Y_{\ell}^m(\theta, \varphi), \quad (9)$$

where b_{ℓ}^m are the expansion coefficients and the spherical harmonics Y_{ℓ}^m are functions of the associated Legendre polynomials P_{ℓ}^m ,

$$Y_{\ell}^m(\theta, \varphi) = K_{\ell}^m P_{\ell}^m(\cos \theta) e^{im\varphi}, \quad (10)$$

with

$$K_{\ell}^m = \sqrt{\frac{2\ell+1}{4\pi} \frac{(\ell-m)!}{(\ell+m)!}}. \quad (11)$$

Multiplying Equation (9) by the complex conjugate of the spherical harmonic, Y_{ℓ}^{m*} , and integrating over the solid angle, the expansion coefficient is found to be

$$b_{\ell}^m = \int_0^{2\pi} d\varphi \int_0^{\pi} d\theta \sin \theta r_{\text{sh}}(\theta, \varphi) Y_{\ell}^{m*}(\theta, \varphi). \quad (12)$$

For our mode analysis we actually use the pseudo-power coefficients $c_{\ell}^2 \equiv |b_{\ell}^0|^2$ and

$$c_{\ell}^2 \equiv \frac{1}{2\ell+1} \left(|b_{\ell}^0|^2 + 2 \sum_{m=1}^{m=\ell} |b_{\ell}^m|^2 \right) \quad (13)$$

for $\ell > 0$, respectively, whose values do not depend on the particular choice of the orientation of the coordinate grid in 3D. The c_{ℓ}^2 are related to the coefficients a_{ℓ}^m of the real spherical harmonics decomposition in Equation (1) by

$$c_{\ell}^2 \equiv 4\pi \sum_{m=-\ell}^{m=\ell} |a_{\ell}^m|^2. \quad (14)$$

In Figure 9 logarithmic values of c_{ℓ}^2 normalized by c_0^2 are plotted.

The north polar and south polar entropy profiles of the 2D simulations in the upper panels of Figure 9 show that the slow contraction case, S25-1, does not explode within 500 ms after bounce, whereas the fast contraction models S25-2 and S25-3 develop explosions around 300 ms post bounce because of the stronger neutrino heating by higher boundary and, in particular, accretion luminosities. The dynamics of the shock and postshock flow until the explosions set in reveals interesting differences in all three cases.

The north and south polar shock trajectories as well as the maximum and minimum shock radii (given by dotted lines in the panels on the second line of Figure 9) in all three 2D cases exhibit pronounced sloshing motions, which suggest considerable activity on the scale of low-order spherical harmonics modes. The most regular pattern of alternating north-polar and south-polar shock expansions and contractions, however, is visible in model S25-2, whose periodic shock excursions remind one strongly of the clean SASI sloshing mode found for the $27 M_{\odot}$ progenitor by Müller et al. (2012a). Before large-amplitude shock motions are reached, the sloshing amplitude grows slowly in an otherwise seemingly quiet environment. A similar behavior was observed by Scheck et al. (2008) in their 2D models W00 and W00F, whose parameter settings (chosen core contraction rate

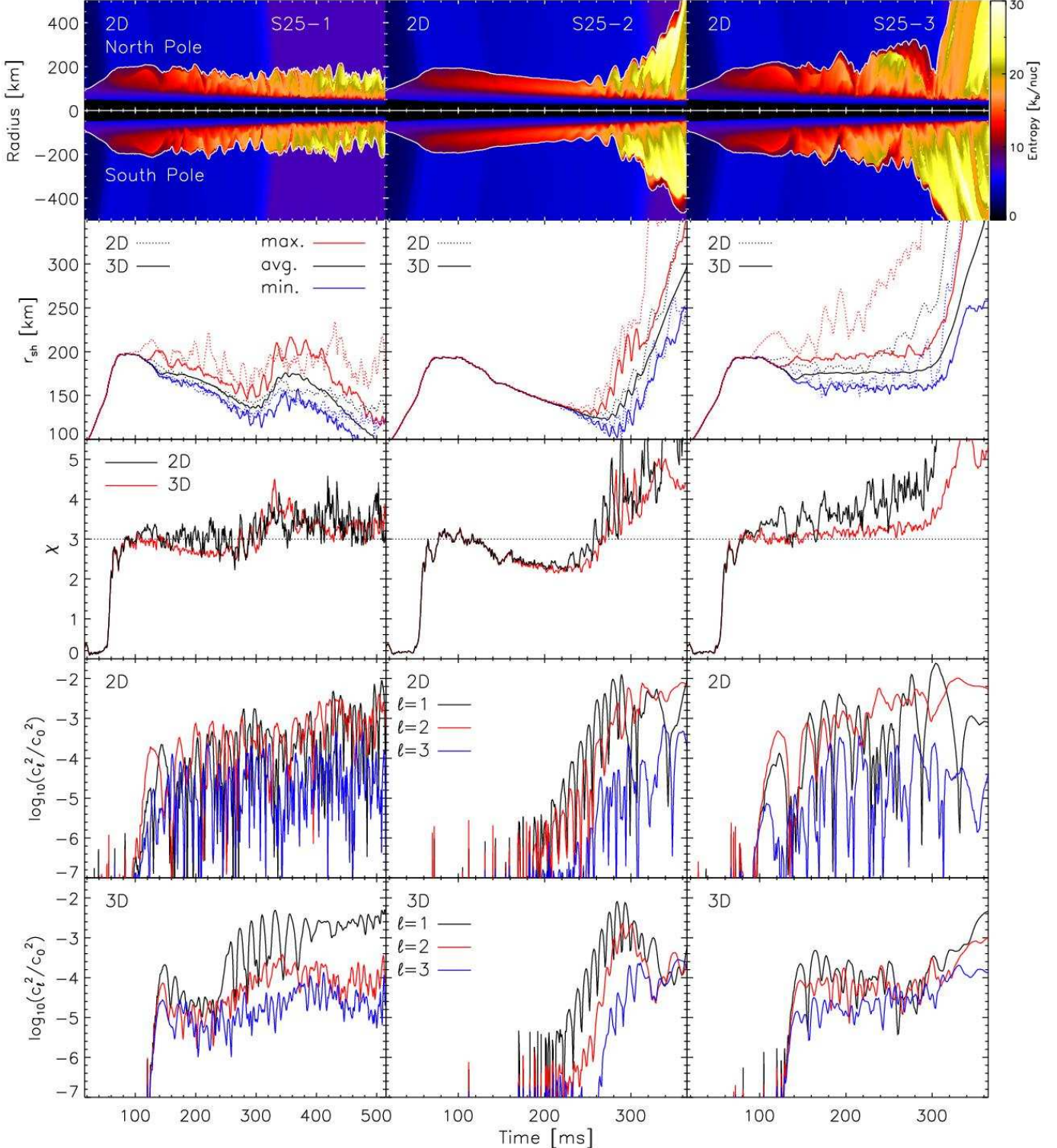


Figure 9. Comparison of the time evolution of 2D and 3D results of our set of parametrized postbounce simulations S25-1, S25-2, and S25-3 of the $25 M_\odot$ progenitor. The upper panels show north polar and south polar entropy profiles for the 2D runs with thin white lines indicating the shock trajectories, which separate low-entropy preshock matter (black and blue) from the high-entropy postshock region (red, orange, yellow). The second panels from the top display maximum, average, and minimum shock radii for 2D (dotted) and 3D models, the panels in the third line present the χ parameter for convective instability (Equation 7) of 2D (black lines) and 3D (red lines) cases, and the plots in the fourth and fifth lines provide the normalized pseudo-power coefficients c_ℓ^2/c_0^2 (Equation 13) on a logarithmic scale for the 2D and 3D simulations, respectively. Phases with values of $\chi \lesssim 3$ correlate with preferred growth of low-mode ($\ell = 1, 2$) SASI activity.

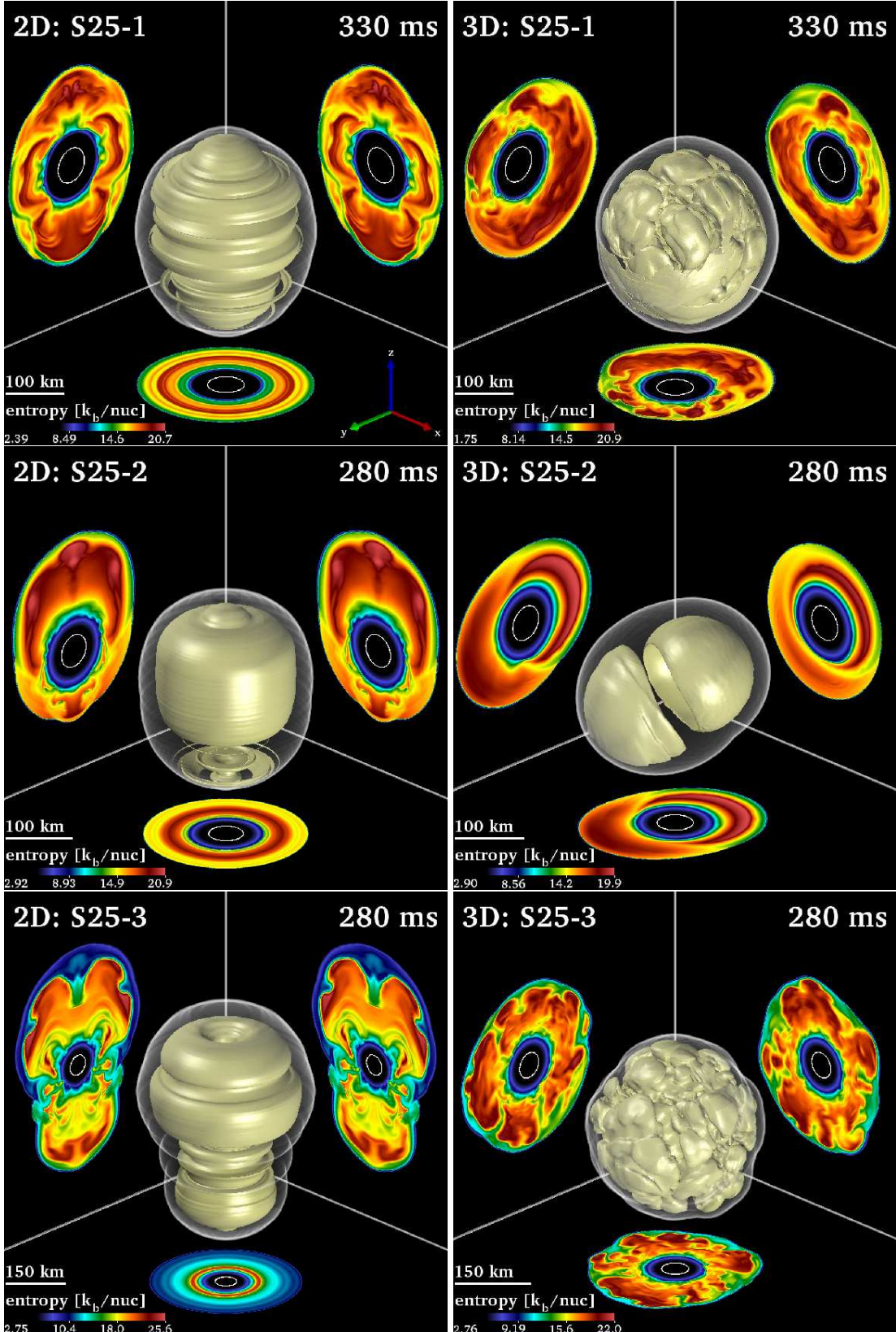


Figure 10. Structure of the 2D (left) and 3D (right) models of our set of parametrized $25 M_{\odot}$ simulations (top: S25-1; middle: S25-2; bottom: S25-3) at representative postbounce times (as given in the upper right corner of each panel). The central object in all panels provides a three-dimensional visualization of the supernova shock (white, transparent surface), which engulfs a surface of constant entropy of $17 k_B$ per nucleon. The images on the cube walls show entropy distributions (the color coding as given by the color bars in the lower left corners with black, blue, and green signaling low values) in the x - y , x - z , and y - z planes (orientation according to triad in the lower right corner of the upper left panel). The white circle indicates the inner grid boundary and a scale stick in each panel gives a measure of the size of the displayed volume. While the 3D model of S25-1 exhibits signatures of neutrino-driven convection and of low-order multipole asymmetry due to SASI shock sloshing, both the 2D and 3D cases of S25-2 show a clear dominance of SASI activity, whereas model S25-3 possesses the clearest pattern of neutrino-driven buoyancy.

in combination with very low core-boundary luminosities) were initially disfavorable for the onset of neutrino-driven convection and thus allowed one to follow the SASI growth from the linear to the nonlinear regime in a very clear way.

In contrast, the 2D models of S25-1 and S25-3 show shorter-timescale variability of the shock trajectories superimposed on a longer-timescale quasiperiodic north-south sloshing of the shock. This suggests the presence of asymmetries of higher-order spherical harmonics type as they are typical of neutrino-driven buoyant plumes.

These descriptions are supported by a more quantitative analysis of the growth conditions of convective instability in the postshock accretion layer as expressed by the critical χ parameter, which measures the ratio of average advection timescale of the accretion flow through the gain region to the convective growth timescale. Inspecting the panels in the third line of Figure 9, where the black curves display the 2D results, reveals that only in model S25-2 χ drops below the critical threshold value of 3 for most of the postbounce evolution until strong shock expansion and explosion sets in. The low values of χ are a consequence of the strong shock contraction in response to the rapidly shrinking core of the neutron star assumed in this model. As expected from the linear perturbation analysis of Foglizzo et al. (2006), which is applicable to model S25-2 because of the small amplitude of the initial seed perturbations, convective overturn cannot develop and the model exhibits the observed clean SASI growth pattern. Correspondingly, the spherical harmonics decomposition of the shock deformation shows the characteristic oscillatory growth of dominant $\ell = 1$ (dipole) and $\ell = 2$ (quadrupole) modes to nonlinear magnitudes over a timescale of roughly 100 ms (fourth panel from top in the middle column of Figure 9).

In contrast, the 2D models of S25-1 and S25-3 show a growth of the shock asymmetries that differs from that of S25-2. A long-time oscillatory rise of the amplitude is not visible in both cases, but relatively large shock deformation develops much earlier and the time dependence of the spherical harmonics amplitudes of order $\ell = 1, 2, 3$ is much more irregular than in S25-2. Although still dipolar and quadrupolar shock deformation modes dominate, the short-timescale variability suggests bubbles and plumes on the smaller angular scales typically connected to the occurrence of strong buoyancy activity in the neutrino-heating layer. This is in agreement not only with χ values around the critical number of 3 for S25-1 and values well above 3 for S25-3, but it is also compatible with the visual impression of the entropy structures between shock and gain radius displayed in the left panels of Figure 10. The pronounced deformation along the symmetry axis, which is responsible for the dominance of the dipolar mode in many evolution phases of all three models, can be nicely seen in the shape of the shock and of the surface of constant entropy displayed by the central, three-dimensional representation of the 2D model structure in each of the left panels. It should be noted, however, that different from the situation of S25-1 and S25-3, where the entropy surface shows short-wavelength variations reflecting the presence of buoyant plumes, this surface is much smoother in model S25-2, where the violent SASI sloshing at 280 ms post bounce is accompanied by much weaker convection.

The rapid onset of buoyancy in models S25-1 and S25-3 is fostered by the larger initial seed perturbations. Since the difference between S25-2 and S25-3 is *only* the size of the amplitude of the initial random seeds (0.1% for S25-2 and 3% for S25-3), the different evolution of the flow asymmetries and the different values of χ in these two models clearly demonstrate the important influence of the magnitude of preexisting deviations from spherical symmetry in the collapsing stellar core.

A comparison of 2D and 3D results for the same modeling setup is extremely interesting now. Inspecting the right panels of Figure 10 it becomes obvious that the SASI activity appears in a much clearer way in the entropy surfaces of the 3D models. The shock sloshing creates smooth, coherent hemispheric shells of constant entropy like those we have seen in Figure 1 and already discussed in Sect. 2.2. The 3D case of S25-2 exhibits such bipolar hemispheric entropy lobes, which are nearly axisymmetric around a direction tilted relative to the three coordinate axes (indicated by the triad), but which possess hardly any substructure on shorter wavelength scales. This indicates that the entropy variations are created by pure SASI sloshing movements of the shock. The three x - y , x - z , and y - z cuts displayed on the cube walls yield an impressive confirmation of nearly perfect entropy half-shells without any indication of secondary, parasitic instabilities of Rayleigh-Taylor or Kelvin-Helmholtz type. In contrast, model S25-3 shows the familiar cauliflower pattern of expanding and fragmenting Rayleigh-Taylor fingers and Kelvin-Helmholtz swirls typical of neutrino-driven buoyancy. Model S25-1 is again different and characterized by features of both types in superposition: The snapshot of the upper right panel in Figure 10 displays a convective bubble pattern that is engulfed by a smooth half-shell closer behind the shock in one hemisphere.

These differences are reflected by the spherical harmonics amplitudes for the $\ell = 1, 2, 3$ modes of the shock deformation in the 3D models presented in the bottom panels of Figure 9. While in models S25-1 and S25-2 the $\ell = 1$ deformation around the times of the snapshots in Figure 10 (330 ms and 280 ms, respectively) remains clearly dominant for longer evolution phases, and the time variation of the dipole amplitude reveals very stable periodicity for 100 ms and more, all three lowest-order spherical harmonics have similar strength in model S25-3 around 280 ms after bounce. In S25-3 the dipolar asymmetry component has the largest amplitude only for some short episodes of the postbounce evolution, although quasi-periodic $\ell = 1$ amplitude variations can be observed also in this case. The higher-order multipoles in all models show greater variation frequencies and less good temporal regularity and seem to be influenced by the stochasticity associated with convective mass motions.

The χ parameter (panels in the third line of Figure 9) aids a better understanding of the differences between the 3D models and of their differences relative to the corresponding 2D results. In the 2D and 3D cases of model S25-2 the values of the χ parameter evolve essentially identically until ~ 250 ms and stay below the critical threshold of 3 for convection for most of the time. Correspondingly, both the 2D and 3D simulations do not develop any significant level of convective activity.

Therefore pure SASI activity can be observed, which in both cases grows in a very similar way and is characterized by a dipolar shock deformation mode that amplifies most rapidly and that dominates the $\ell = 2, 3$ spherical harmonics components in 3D even more than in 2D.

In model S25-3, which differs from S25-2 only in the size of the initial seed perturbations, the quick appearance of buoyancy asymmetries leads to a stronger shock expansion, which prevents χ from dropping below 3 in both the 2D and 3D runs. In this case SASI activity cannot be unambiguously diagnosed by persistent shock sloshing or spiraling. The amplitudes of the $\ell = 1, 2, 3$ shock deformation modes in 3D remain fairly small (much smaller than the maximum amplitudes of S25-1 and S25-2), and a clear hierarchy of these lowest-order multipoles over longer periods of time is not established in the 3D case of S25-3 (Figure 9, bottom right panel).

Models S25-2 and S25-3 in comparison confirm that the growth conditions of SASI activity improve in phases of strong shock contraction. As discussed in Scheck et al. (2008), the SASI growth rate roughly scales inversely with the advection timescale of the accretion flow from the shock to the neutron-star surface. In model S25-3 the stronger shock expansion, triggered by convection that is seeded by the (nonlinear) initial perturbations, leads to longer advection times and thus disfavors the development of the SASI.

Model S25-1 demonstrates another interesting effect. The SASI can be stronger in 3D models than in the corresponding 2D cases. In the 3D version of S25-1 the shock deformation mode develops a very large $\ell = 1$ amplitude, for which after 250 ms c_1^2 exceeds the amplitudes of the higher-order multipoles by more than an order of magnitude (Figure 9, bottom left panel). While quasiperiodic shock oscillations with nice regularity and nearly stable axis characterize the evolution until about 350 ms, the direction of the dipole axis wanders afterward to give way to a strengthening spiral mode after ~ 500 ms, which coincides with the phase of most extreme shock recession. In the 3D case the SASI activity appears much more strongly than in 2D, where dipolar and quadrupolar deformation modes have similar size and higher multipoles, associated with convective mass motions, contribute significantly. The relevance of convection in the 2D model is compatible with the χ being around 3 in this case, whereas $\chi < 3$ in the 3D run reduces the influence of buoyancy but signals more favorable conditions for the SASI because of a shorter advection timescale (similar to the situation in S25-2).

It is important to note that both S25-1 and S25-3 were computed with large initial seed perturbations. In the case of S25-3, however, the larger boundary and accretion luminosities lead to stronger neutrino heating, which supports buoyancy and allows the shock radius to stay large even in the 3D case. On the contrary, in S25-1 the weaker neutrino heating does not prevent shock retraction.

Convection and SASI activity in 3D therefore depend sensitively on the behavior of the accretion shock, which in turn reacts to the neutron star contraction and the power of neutrino-energy deposition. Our set of models shows that for a favorable combination of conditions the SASI in 3D can be much stronger (S25-1) and purer

(S25-2) than in the corresponding 2D cases. In general, however, the development of convection and SASI in the postshock accretion layer seems to be fully compatible with the general theoretical understanding obtained in connection of 2D hydrodynamic simulations in Scheck et al. (2008).

4. DISCUSSION AND CONCLUSIONS

We have simulated the post-bounce evolution of the $27 M_\odot$ progenitor of Woosley et al. (2002) in 2D and 3D, using the PROMETHEUS-VERTEX code with detailed multi-group neutrino transport including the full, sophisticated set of neutrino reactions applied previously in 1D and 2D supernova modeling by the Garching group. Moreover, we performed a set of 2D and 3D post-bounce simulations of the $25 M_\odot$ progenitor of Woosley et al. (2002) with the PROMETHEUS hydrodynamics scheme and a computationally efficient, gray neutrino transport approximation, employing a parametric approach in which an inner grid boundary replaced the excised high-density core of the proto-neutron star and allowed us to more systematically explore the influence of different core neutrino luminosities and of faster or slower contraction of the forming remnant. We emphasize that this approach is different from that for our $27 M_\odot$ runs, where the whole neutron star to the center was included in the computational domain. In addition, we also tested the effects of varied amplitudes of random perturbations that had to be imposed for seeding the growth of nonradial hydrodynamic instabilities in the neutrino-heated accretion layer behind the stalled supernova shock. While the 3D run for the $27 M_\odot$ star was conducted with a polar coordinate grid, an axis-free Yin-Yang grid was used in the studies of the $25 M_\odot$ progenitor.

Our simulations for the first time provide unambiguous evidence of the occurrence of large-amplitude SASI shock sloshing and spiral motions and of their interplay with neutrino-driven convection in 3D supernova core environments modeled with a “realistic” treatment of neutrino transport and the corresponding heating and cooling effects. Previous hydrodynamic studies had been able to identify SASI activity, and in particular SASI spiral modes, only in 3D setups with adiabatic postshock accretion flows (Blondin & Mezzacappa 2007; Fernández 2010) and in some simulations with a simple neutrino light-bulb treatment (Iwakami et al. 2008, 2009). The shallow water analogue of the SASI was also observed experimentally, however again without the presence of buoyancy motions (Foglizzo et al. 2012). On the basis of more recent 3D simulations with a simple neutrino light-bulb approximation (Burrows et al. 2012; Murphy et al. 2012; Dolence et al. 2013) and 3D GR models with a neutrino leakage scheme (Ott et al. 2012) it was even concluded that the SASI is at most of minor relevance for the dynamics of the postshock layer in collapsing stellar cores (see also Burrows 2013).

Our findings indicate that the SASI is potentially much more important in 3D than suggested by these previous investigations. Besides the core-density profile of the progenitor star, which determines the temporal evolution of the mass infall rate, the more elaborate neutrino transport treatment (in particular in our $27 M_\odot$ simulation) may partly be responsible for the different accretion-flow dynamics seen in our models. The details of the neutrino

description are relevant, because they can cause differences in the contraction behavior of the proto-neutron star and in the neutrino-heating in the gain layer. Both affect the evolution of the stagnation radius of the accretion shock and thus have a strong impact on the growth conditions for convection and the SASI. In the artificial setup used by Burrows et al. (2012); Murphy et al. (2012); Dolence et al. (2013), the neutron star is not allowed to deleptonize and radiate energy, therefore its radius stays unrealistically large (50–60 km) during the whole simulated postbounce evolution (up to ~ 1 s). Also the leakage scheme of Ott et al. (2012), which can track the contraction of the proto-neutron star and the time evolution of the neutrino emission to a certain extent, deviates significantly from full transport models. For example, in the work of Ott et al. (2012) the mean energy of the radiated electron neutrinos around 100 ms after core bounce is more than 60% higher than that found with the VERTEX transport code by Müller et al. (2012a), although both groups investigated the same $27 M_{\odot}$ progenitor with relativistic methods. It is clear that the neutrino heating found by Ott et al. (2012) was stronger and thus more favorable for larger shock radii, which in turn was supportive of neutrino-driven convection instead of the SASI.

In contrast to the findings by Burrows et al. (2012); Murphy et al. (2012); Dolence et al. (2013) and by Ott et al. (2012), we observe strong SASI activity in our 3D simulations both for the $27 M_{\odot}$ progenitor and the $25 M_{\odot}$ star. The SASI can become the clearly strongest nonradial instability during at least some parts of the evolution and can be clearly identified by its oscillatory growth properties and even in the nonlinear regime by its characteristic low-order spherical harmonics modes of coherent shock motion and shock deformation. In detail, we can draw the following conclusions from our models:

- SASI activity can develop in 3D despite and in addition to the earlier presence of neutrino-driven buoyancy. Different from the higher-order multipole pattern that is typical of convective plumes and downdrafts, the SASI reveals itself by coherent, large-amplitude shock sloshing and spiral motions.
- Because of the absence of a flow-constraining symmetry axis, which also directs the structure of neutrino-driven buoyancy in 2D models, SASI shock motions and deformation modes can be recognized more easily and more clearly in the 3D case. Interestingly, both the $27 M_{\odot}$ and $25 M_{\odot}$ models exhibit evolution phases in which the SASI in 3D can become stronger than in the corresponding 2D runs. The dominance of the SASI and greater strength in 3D can be concluded not only from the large dipole and quadrupole amplitudes of the shock deformation, but also from the higher nonradial kinetic energy of the postshock flow (Figure 2) and from a prominent peak at low-order multipoles in the power spectrum of the nonradial kinetic energy (Figure 3). While some authors hypothesized (Iwakami et al. 2008) that the SASI amplitudes in 3D remain smaller than those in 2D because the kinetic energy of the nonradial flow is shared with an additional degree of freedom, our results suggest that there is no such limitation of the kinetic energy that can be stored in lateral and azimuthal mass motions. The fraction of the huge reservoir of accretion energy that is converted to nonradial flows in the postshock layer can be larger in 3D than in 2D.
- Depending on the conditions in the postshock flow, which in our $25 M_{\odot}$ runs could be controlled by the choices of the contraction behavior and neutrino luminosities assumed at the inner grid boundary, phases of essentially *pure* SASI activity could be obtained, with neutrino-driven convection only developing as the secondary instability (cf. Figure 10, middle panels). This result of the 2D and 3D models of the present work is very similar to the flow behavior seen in the 2D simulation of the $27 M_{\odot}$ progenitor by Müller et al. (2012a).
- The growth of the SASI is favored by fast advection flows, because its growth rate in an advective-acoustic cycle scales roughly inversely with the advection timescale of the accretion flow from the shock to the neutron star surface (e.g., Scheck et al. 2008). This is opposite to neutrino-driven buoyancy, whose growth in the accretion flow requires that the critical ratio χ of advection timescale to buoyancy timescale exceeds a value of about 3 (Foglizzo et al. 2006). Fully consistent with this dimension-independent theoretical understanding, which was developed by linear analysis and hydrodynamical modeling in 2D, we find SASI growth also in the 3D case to be strongest in phases of small shock stagnation radii, which are connected to rapidly shrinking and more compact proto-neutron stars as well as relatively weak neutrino heating.
- Also the amplitude of the initial seed perturbations (of the density or velocity field) is found to potentially have an influence. A greater amplitude can trigger a faster development of neutrino-driven convection (for perturbations of nonlinear size this can happen even when $\chi < 3$, see Scheck et al. 2008). If the buoyancy instability is supported by sufficiently strong neutrino heating to instigate an expansion of the shock, SASI growth can become disfavored and nonradial flows in the postshock layer are dominated by buoyant plumes and downflows.
- Preferentially in phases of strongest shock recession we observe bipolar ($\ell = 1, m = 0$) SASI sloshing motions to change over to a spiral ($\ell = 1, m = 1$) mode in the 3D simulations of both the $27 M_{\odot}$ and $25 M_{\odot}$ models (Figures 6 and 7). The transition to the time-dependent rotating shock-deformation pattern therefore seems to be favored by particularly small shock radii. In general, the character of the 3D accretion flow during shock oscillation and spiraling phases with wandering directions reveals close similarity to the behavior of the hydraulic jump observed in the SWASI experiment (Foglizzo et al. 2012).

Our comparison of the SASI activity in the 2D and 3D simulations of the $27 M_{\odot}$ model, which was evolved

fully self-consistently (i.e., without the use of free parameters and without an inner grid boundary) is particularly interesting. It revealed that at an early stage, when the mass accretion rate is still high and the shock correspondingly retreats in response to the proto-neutron star contraction, the SASI can grow despite some prior neutrino-driven convective activity. Before the accretion of the Si/SiO interface, the SASI can reach even higher amplitudes in 3D than in 2D. The large-amplitude shock-sloshing mode eventually makes the transition to a spiral mode in 3D, which, however, is quenched around 260 ms after bounce once the accretion rate has dropped significantly and the shock has expanded to radii of nearly 200 km on average. Despite the faster shock expansion and higher kinetic energy of the postshock flow, the 3D model nevertheless falls short of an explosive runaway unlike the 2D simulation.

A discussion of this important difference in the explosion behavior of 2D and 3D models, which is fully consistent with the results obtained by Hanke et al. (2012), is beyond the scope of this paper and will be addressed in future work. We do not want to speculate here about the relevance of the SASI in competition with neutrino-driven convection for getting explosions in 3D. It is possible that the SASI could provide crucial support for the onset of the explosion, especially since a very strong spiral mode returns towards the end of our $27 M_{\odot}$ simulation. Such a SASI supported explosion was obtained in our parametric $25 M_{\odot}$ simulation of model S25-2 (Figure 9, middle column). But it is also possible that its presence is only temporary and that neutrino-driven convection dominates when the explosion sets in and the preceding shock expansion leads to disfavorable conditions for the advective-acoustic cycle feeding the SASI. Even in the latter case, the SASI could still play an essential role in the explosion mechanism by pushing out the shock far enough for convection to take over in cases where convection cannot develop on its own in an initially stabilized post-shock flow. The conditions for the growth and long-time persistence of the SASI, in particular of the spiral mode, are still poorly understood and have to be explored in more detail by future 3D simulations. Our results suggest that the exact role of the SASI will depend strongly and in a subtle way not only on a variety of progenitor dependent conditions like the steepness of the density profile, the location and sharpness of the composition shell interfaces, the existence of initial non-radial asymmetries in the collapsing stellar core, angular momentum of the progenitor core, which could trigger a faster growth of the spiral mode even for small rotation rates (Yamasaki & Foglizzo 2008), and magnetic fields, if these are amplified to dynamically relevant strength. The SASI growth conditions will also depend on the contraction behavior of the nascent neutron star, which is influenced by its high-density equation of state and by general relativistic gravity, and on the strength of the neutrino heating, whose determination requires a sophisticated treatment of the energy-dependent neutrino transport.

The initial perturbations constitute a potential cause for differences that is very difficult to address. Certainly neither the artificially imposed random perturbations in our models, nor the small intrinsic numerical seeds of Müller et al. (2012a), nor the larger intrinsic per-

turbations in the simulations of Ott et al. (2012) reflect the magnitude and spectral shape of the physical perturbations present in realistic progenitors. In the end, a well-founded understanding of the interplay between convection and the SASI will probably require multi-dimensional progenitor models.

If we suppose that the growth conditions for the SASI remain favorable for realistic seed perturbations, our self-consistent 3D model of the $27 M_{\odot}$ progenitor still throws up a number of further questions: Has the SASI already reached its saturation level in our model, or could it grow further if massive accretion were to last longer? Could it play a decisive dynamical role for reaching an explosive runaway in the latter case, even if it is only by pushing the shock out far enough for convection to take over later? Are the saturation properties of the nonlinear spiral mode different from the nonlinear sloshing mode because of the different geometry of the down-flows and the presence of considerable angular momentum in the gain region? If the strong and clear spiral mode survives until the onset of an explosion, what would be its final impact on the proto-neutron star kick and spin? What are the neutrino-emission variations connected to large-amplitude shock sloshing and spiral motions in the 3D case? Are these signal variations observable with a similar strength as predicted for the 2D case (see Marek & Janka 2009; Lund et al. 2010)? With sophisticated 3D supernova modeling only now beginning to become feasible, our understanding of 3D effects in supernova cores is still in its infancy, and further research into the properties of the SASI is urgently needed.

We are grateful to Elena Erastova and Markus Rampp (Rechenzentrum Garching) for visualizing the 3D simulation in Figure 1. This research was supported by the Deutsche Forschungsgemeinschaft through the Transregional Collaborative Research Center SFB/TR 7 “Gravitational Wave Astronomy” and the Cluster of Excellence EXC 153 “Origin and Structure of the Universe” (<http://www.universe-cluster.de>). The results described in this paper could only be achieved with the assistance of high performance computing resources (Tier-0) provided by PRACE on CURIE TN (GENCI@CEA, France) and SuperMUC (GCS@LRZ, Germany). We also thank the Rechenzentrum Garching for computing time on the IBM iDataPlex system *hydra*.

REFERENCES

- Arcones, A., & Janka, H.-T. 2011, A&A, 526, A160
- Arcones, A., Janka, H.-T., & Scheck, L. 2007, A&A, 467, 1227
- Bethe, H. A. 1990, Rev. Mod. Phys., 62, 801
- Blondin, J. M., & Mezzacappa, A. 2006, ApJ, 642, 401
- . 2007, Nature, 445, 58
- Blondin, J. M., Mezzacappa, A., & DeMarino, C. 2003, ApJ, 584, 971
- Brandt, T. D., Burrows, A., Ott, C. D., & Livne, E. 2011, ApJ, 728, 8
- Buras, R., Janka, H.-T., Rampp, M., & Kifonidis, K. 2006a, A&A, 457, 281
- Buras, R., Rampp, M., Janka, H.-T., & Kifonidis, K. 2006b, A&A, 447, 1049
- Burrows, A. 2013, Reviews of Modern Physics, 85, 245
- Burrows, A., Dolence, J. C., & Murphy, J. W. 2012, ApJ, 759, 5
- Burrows, A., & Fryxell, B. A. 1992, Science, 258, 430
- Burrows, A., & Hayes, J. 1996, Physical Review Letters, 76, 352

Burrows, A., Hayes, J., & Fryxell, B. A. 1995, ApJ, 450, 830

Colella, P., & Woodward, P. R. 1984, *J. Comp. Phys.*, 54, 174

Couch, S. M. 2012, ArXiv:1212.0010

Dolence, J. C., Burrows, A., Murphy, J. W., & Nordhaus, J. 2013, ApJ, 765, 110

Ellis, J., Janka, H.-T., Mavromatos, N. E., Sakharov, A. S., & Sarkisyan, E. K. G. 2012a, Phys. Rev. D, 85, 045032

—. 2012b, Phys. Rev. D, 85, 105028

Fernández, R. 2010, ApJ, 725, 1563

Fernández, R., & Thompson, C. 2009a, ApJ, 703, 1464

—. 2009b, ApJ, 697, 1827

Foglizzo, T. 2002, A&A, 392, 353

Foglizzo, T., Galletti, P., Scheck, L., & Janka, H.-T. 2007, ApJ, 654, 1006

Foglizzo, T., Masset, F., Guilet, J., & Durand, G. 2012, Physical Review Letters, 108, 051103

Foglizzo, T., Scheck, L., & Janka, H.-T. 2006, ApJ, 652, 1436

Fryer, C. L., & Heger, A. 2000, ApJ, 541, 1033

Fryxell, B. A., Müller, E., & Arnett, D. 1989, Max-Planck-Institut für Astrophysik, Preprint0, 449

Guilet, J., & Foglizzo, T. 2012, MNRAS, 421, 546

Hanke, F., Marek, A., Müller, B., & Janka, H.-T. 2012, ApJ, 755, 138

Herant, M. 1995, Phys. Rep., 256, 117

Herant, M., Benz, W., & Colgate, S. 1992, ApJ, 395, 642

Herant, M., Benz, W., Hix, W. R., Fryer, C. L., & Colgate, S. A. 1994, ApJ, 435, 339

Iwakami, W., Kotake, K., Ohnishi, N., Yamada, S., & Sawada, K. 2008, ApJ, 678, 1207

—. 2009, ApJ, 700, 232

Janka, H.-T., Hanke, F., Hüdepohl, L., Marek, A., Müller, B., & Obergaulinger, M. 2012, Progress of Theoretical and Experimental Physics, 2012, 010000

Janka, H.-T., & Müller, E. 1994, A&A, 290, 496

—. 1996, A&A, 306, 167

Kifonidis, K., Plewa, T., Janka, H.-T., & Müller, E. 2003, A&A, 408, 621

Kifonidis, K., Plewa, T., Scheck, L., Janka, H.-T., & Müller, E. 2006, A&A, 453, 661

Kitaura, F. S., Janka, H.-T., & Hillebrandt, W. 2006, A&A, 450, 345

Kuroda, T., Kotake, K., & Takiwaki, T. 2012, ApJ, 755, 11

Laming, J. M. 2007, ApJ, 659, 1449

Lattimer, J. M., & Swesty, F. D. 1991, *Nucl. Phys. A*, 535, 331

Lund, T., Marek, A., Lunardini, C., Janka, H., & Raffelt, G. 2010, Phys. Rev. D, 82, 063007

Lund, T., Wongwathanarat, A., Janka, H.-T., Müller, E., & Raffelt, G. 2012, Phys. Rev. D, 86, 105031

Marek, A., Dimmelmeier, H., Janka, H.-T., Müller, E., & Buras, R. 2006, A&A, 445, 273

Marek, A., & Janka, H. 2009, ApJ, 694, 664

Marek, A., Janka, H., & Müller, E. 2009, A&A, 496, 475

Müller, B., Janka, H.-T., & Heger, A. 2012a, ApJ, 761, 72

Müller, B., Janka, H.-T., & Marek, A. 2012b, ApJ, 756, 84

—. 2013, ApJ, 766, 43

Müller, E., & Janka, H.-T. 1997, A&A, 317, 140

Müller, E., Janka, H.-T., & Wongwathanarat, A. 2012c, A&A, 537, A63

Murphy, J. W., & Burrows, A. 2008, ApJ, 688, 1159

Murphy, J. W., Dolence, J. C., & Burrows, A. 2012, ArXiv:1205.3491

Murphy, J. W., Ott, C. D., & Burrows, A. 2009, ApJ, 707, 1173

Nordhaus, J., Brandt, T. D., Burrows, A., & Almgren, A. 2012, MNRAS, 2901

Nordhaus, J., Brandt, T. D., Burrows, A., Livne, E., & Ott, C. D. 2010a, Phys. Rev. D, 82, 103016

Nordhaus, J., Burrows, A., Almgren, A., & Bell, J. 2010b, ApJ, 720, 694

Ott, C. D., Burrows, A., Dessart, L., & Livne, E. 2008, ApJ, 685, 1069

Ott, C. D., et al. 2012, ArXiv:1210.6674

Rampp, M., & Janka, H.-T. 2002, A&A, 396, 361

Scheck, L., Janka, H.-T., Foglizzo, T., & Kifonidis, K. 2008, A&A, 477, 931

Scheck, L., Kifonidis, K., Janka, H.-T., & Müller, E. 2006, A&A, 457, 963

Scheck, L., Plewa, T., Janka, H.-T., Kifonidis, K., & Müller, E. 2004, Physical Review Letters, 92, 011103

Suwa, Y., Kotake, K., Takiwaki, T., Whitehouse, S. C., Liebendörfer, M., & Sato, K. 2010, PASJ, 62, L49+

Takiwaki, T., Kotake, K., & Suwa, Y. 2012, ApJ, 749, 98

Uglio, M., Janka, H.-T., Marek, A., & Arcones, A. 2012, ApJ, 757, 69

Wongwathanarat, A., Hammer, N. J., & Müller, E. 2010a, A&A, 514, A48

Wongwathanarat, A., Janka, H., & Müller, E. 2010b, ApJ, 725, L106

Wongwathanarat, A., Janka, H.-T., & Mueller, E. 2012, ArXiv:1210.8148

Woosley, S. E., Heger, A., & Weaver, T. A. 2002, Rev. Mod. Phys., 74, 1015

Yamasaki, T., & Foglizzo, T. 2008, ApJ, 679, 607

Yamasaki, T., & Yamada, S. 2007, ApJ, 656, 1019